Laser-induced fluorescence velocity measurements of a diverging cusped-field thruster

IOP Publishing Journal of Physics D: Applied Physics
J. Phys. D: Appl. Phys. **44** (2011) 295203 (10pp) doi:10.1088/0022-3727/44/29/295203

Laser-induced fluorescence velocity measurements of a diverging cusped-field thruster

N A MacDonald[1], M A Cappelli[1], S R Gildea[2], M Martínez-Sánchez[2] and W A Hargus Jr[3]

[1] Stanford Plasma Physics Laboratory, Stanford University, Stanford, CA 94305, USA
[2] Space Propulsion Laboratory, Massachusetts Institute of Technology, Cambridge, MA 02139, USA
[3] Spacecraft Propulsion Branch, Air Force Research Laboratory, Edwards AFB, CA 93524, USA

E-mail: smacdo@stanford.edu

Received 6 January 2011, in final form 24 May 2011
Published 30 June 2011
Online at stacks.iop.org/JPhysD/44/295203

Abstract
Measurements are presented of the most probable time-averaged ion velocities within the acceleration channel and in the plume of a diverging cusped-field thruster operating on xenon. Xenon ion velocities for the thruster are derived from laser-induced fluorescence measurements of the $5d[4]_{7/2}$–$6p[3]_{5/2}$ xenon ion excited state transition centred at $\lambda = 834.72$ nm. The thruster is operated in both a high-current mode, where the anode discharge current is shown to oscillate periodically, and a low-current mode where operation is relatively quiescent. In the low-current mode, ion emission is predominantly in the form of a conical jet, whereas in the high-current mode, the emission is still divergent but more diffuse throughout the cone angle. These time-average measurements provide insight into the structure of the acceleration region. However, discerning the mechanism for the diffuse ion emission in the strongly oscillating high-current mode will require ion velocity measurements capable of resolving the time-dependent behaviour of the discharge.

(Some figures in this article are in colour only in the electronic version)

1. Introduction

Electric propulsion devices such as Hall thrusters have proven to be an effective alternative to chemical thrusters for applications such as satellite station keeping and primary propulsion systems for deep-space missions [1]. The typical annular Hall thruster employs a crossed radial magnetic field and axial electric field to trap electrons in their channel, ionize propellant and accelerate the ions out of the thruster [2]. A limiting factor for the lifetime of these thrusters is erosion of the electrically insulating channel walls due to heat loading and sputtering from high energy ions [2, 3]. To mitigate erosion, several thruster designs incorporating cusped magnetic field profiles that keep high energy ions away from channel walls are currently being studied. These include the High Efficiency Multi-stage Plasma (HEMP) thruster developed by the THALES Research Institute [4, 5], the Princeton University Cylindrical Hall Thruster (CHT) [6–9], the Massachusetts Institute of Technology (MIT) diverging cusped-field thruster (DCFT) [10] and the Stanford University diverging cusped field (DCF) thruster [11].

The concept of cusped-field thrusters draws from experience with Hall thrusters [6] and travelling wave tubes [12]. Strong permanent ring magnets of alternating polarity are used to form cusped magnetic field features. The magnetic cusps trap and reflect energetic electrons within the volume of the discharge chamber, allowing for enhanced propellant ionization. A strong radial portion of the magnetic field is seen only at magnet interfaces, thereby minimizing ion bombardment and heat dissipation to the walls [4]. Combined with strong electric field gradients that impede electron movement towards the anode [4], cusped-field thrusters accelerate ions with minimal wall interactions. Recent work on cusped field thrusters has shown that they vary greatly from traditional Hall thrusters [6, 13–18]. Cusped-field thrusters tend to have a large portion of their ion acceleration outside

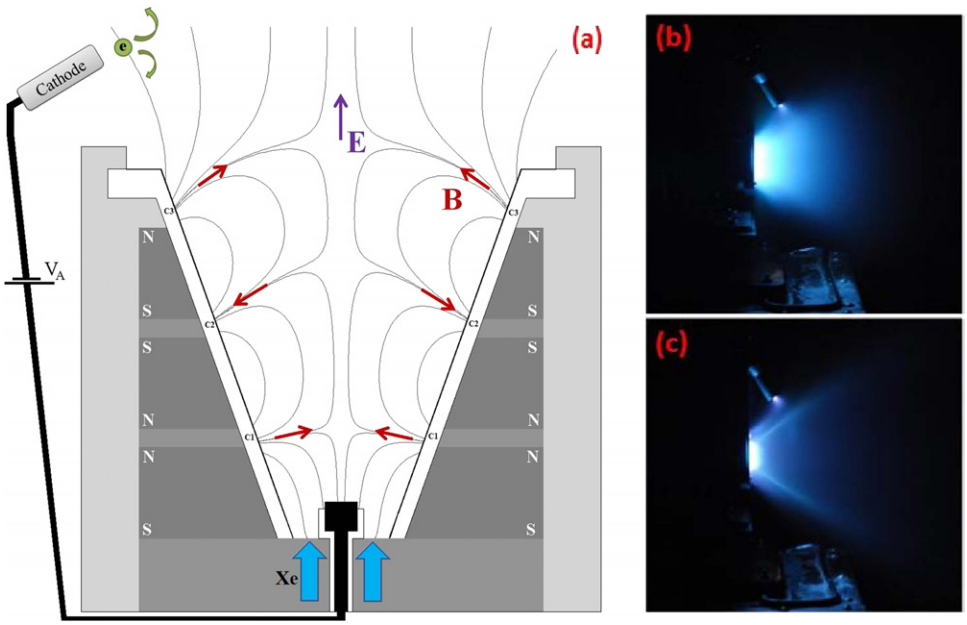

Figure 1. DCFT, developed by MIT. (*a*) Schematic of DCFT, (*b*) operation in high-current mode, (*c*) operation in low-current mode.

of the thruster, and a high divergence angle with radial ion velocities of comparable magnitude to axial ion velocities [14]. Unlike Hall thrusters, the strong magnetic fields seen in cusped-field designs using permanent magnets (≈0.5 T) [19] do not rule out the possibility that ions may be weakly magnetized. Therefore, in some regions of these cusped-field thrusters there could be a significant ion $\vec{E} \times \vec{B}$ drift.

To further understand the operation of cusped-field thrusters, this study seeks to characterize one particular variant, the MIT DCFT, using laser-induced fluorescence (LIF) velocimetry. A survey of the axial velocities within the acceleration channel and axial and radial velocities in the near-field of the plume of the DCFT is presented. The DCFT incorporates permanent magnet rings of alternating polarity to create the cusped magnetic field profile while reducing thruster weight and power consumption by eliminating the magnetic circuit [20]. It has a diverging, cone-shaped channel to further minimize ion bombardment near the exit plane. It also has a hollow, cone-shaped plume [17] where the highest current densities and highest ion velocities appear in a 'jet' at an angle of 30° to 40° from the centreline of the thruster [21].

As described below, time-averaged xenon ion velocities for the thruster are derived from LIF measurements of the $5d[4]_{7/2}$–$6p[3]_{5/2}$ xenon ion excited state transition at $\lambda = 834.72$ nm. The measured spectral feature, which is a convolution of the ion velocity distribution function (VDF), and the transition lineshape, is used to determine the most probable velocities at various positions throughout the thruster channel and in the plume. These velocities are used to determine the ion kinetic energies and to estimate electric field strength along the centreline of the thruster.

2. Experiment

A schematic of the DCFT is shown in figure 1. Details about the permanent magnets (SmCo 3212) and the magnetic field topology can be found elsewhere [16]. The acceleration channel in the DCFT has a diverging, cone shape that is 49.5 mm in depth, 28 mm in radius at the exit plane, with a cone half angle of 22.5° [20]. Permanent magnets of alternating polarity are placed along the channel with decreasing strength as they approach the exit plane. This results in a magnetic field profile that is largely in the axial direction, with radial components at the magnet interfaces (i.e. cusps). The cusped magnetic fields produce a magnetic bottle effect for incoming electrons, trapping them between cusps where they mirror back and forth, allowing for a high ionization percentage and preventing electrons from the external cathode from travelling directly to the anode. This design is intended to reduce erosion and wall losses by preventing the plasma from hitting the channel walls.

The MIT DCFT tends to operate in either a high-current or low- current mode. The high-current mode is characterized by periodic oscillations in the discharge current, while the low-current mode is quiescent, as shown by the anode current traces in figure 2. No voltage data were taken in this particular study. However, previous tests of the DCFT operating in either mode, with voltage sampling rates too slow to fully resolve the wave form, show insignificant variations which would be statistically inconsistent with significant fluctuations.

Based on the current traces in figure 2 and optical observations [18], it appears that the oscillatory nature of the high-current mode can be described by three distinguishable phases within each current cycle:

(i) Fast ionization occurs throughout the region accessible to the plasma, on a fast (electron avalanche) time scale. The neutral population is rapidly consumed in this accessible region.
(ii) Ions are evacuated from the downstream end of the formed plasma, with simultaneous electron evacuation to the anode. The plasma edge recedes at the Bohm velocity

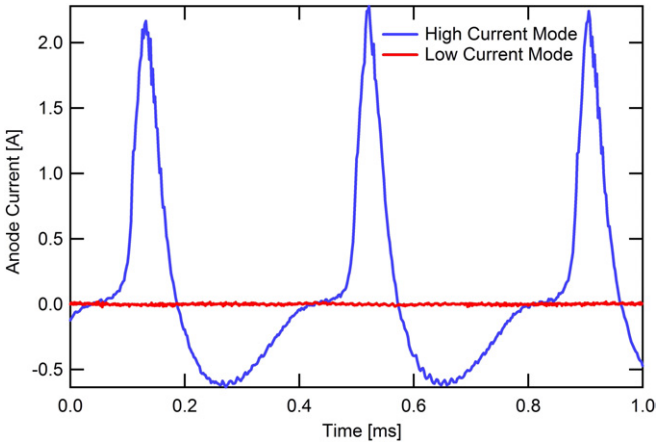

Figure 2. Anode current traces for high- and low-current operating conditions. For the high-current mode, it can be seen that the ionization occurs in short bursts. Plasma luminosity, recorded with a high-speed camera [18], follows the same intensity profile as the anode current traces. Note that the current probe was ac coupled.

(on the order of 3 000 m s^{-1}), taking about 0.015 ms (on the order of the rise time of the anode current pulse) to cover the 50 mm distance from the exit plane to the anode. Additional time is taken to ionize and evacuate neutrals that were left in the inaccessible 'bubbles' between cusps (the observed 0.08 ms of the pulse width).

(iii) The neutrals gradually re-fill the thruster channel. At the estimated 200 m s^{-1} of neutral front advance, this phase covers another 0.25 ms, after which breakdown conditions are again reached and the cycle repeats itself.

It is to be noted that this mode of operation does not necessarily imply a low propellant utilization efficiency, as the ionization of the neutral gas can be nearly complete in each pulse. Based on test data [16] this efficiency is estimated to be 89% for the high current mode.

The specifications for the high- and low-current operating conditions examined in this study are given in tables 1 and 2. The high-current mode, achieved by running the thruster with an 830 μg s^{-1} flow rate and 300 V anode potential, was chosen to match a highly efficient operating condition demonstrated in previous work at MIT [20] while maintaining a power of less than 200 W. The 200 W restriction was imposed to prevent heat loading on the magnets from degrading the magnetic field significantly during long tests.

Transitioning from high- to low-current mode can be achieved by either raising the applied anode voltage or by lowering the propellant flow rate to the anode. The first attempt at operating the thruster in the low-current mode by raising the voltage to 400 V while maintaining 830 μg s^{-1} of flow rate proved unsuccessful, as the thruster reverted back to the high-current mode within about 30 min. To maintain operation in the low-current mode while keeping the operating power less than 200 W, it was necessary to both raise the voltage and lower the anode flow rate. The resulting low-current operating condition used in this study had an anode potential of 400 V and flow rate of 590 μg s^{-1}. Both conditions were run with a background chamber pressure of 5×10^{-6} Torr during thruster operation (corrected for xenon).

Table 1. High-current operating condition.

Anode flow	830 μg s^{-1} (8.5 sccm) Xe
Cathode flow	150 μg s^{-1} (1.5 sccm) Xe
Anode potential	300 V
Anode current	0.53 A
Keeper current	0.50 A
Heater current	3.0 A

Table 2. Low-current operating condition.

Anode flow	590 μg s^{-1} (6.0 sccm) Xe
Cathode flow	150 μg s^{-1} (1.5 sccm) Xe
Anode potential	400 V
Anode current	0.17 A
Keeper current	0.50 A
Heater current	3.0 A

In this experiment, LIF is used to measure the most probable velocities of ions in the thruster channel and plume. LIF is a particularly useful diagnostic for electric propulsion devices such as the DCFT where plasmas create harsh, non-uniform environments.

LIF is a particularly useful diagnostic for plasma propulsion devices which can be highly non-uniform in their discharge structure. LIF provides the opportunity to probe small plasma sources for characterizing ion energy with higher spatial resolution (typically $<$1 mm) than that which can be obtained with intrusive probes such as retarding potential analysers. Finally, the hot, energetic environment can have adverse affects on intrusive probes (e.g. sputtering and melting) and the probes themselves can adversely affect the operation of the discharge. We note, however, that the time-averaged LIF studies carried out here do not resolve ion dynamics due to periodic variations in discharge current and these measurements are therefore seen as a first look into the structure of these cusped-field discharges.

Ion velocity measurements are accomplished by probing the $5d[4]_{7/2}$–$6p[3]_{5/2}$ electronic transition of Xe II at 834.72 nm. The upper state of this transition is shared by the relatively strong $6s[2]_{3/2}$–$6p[3]_{5/2}$ transition at 541.92 nm [22], which is used in this study for non-resonant fluorescence collection. This method mitigates noise induced by surface reflections of the probe beam [22, 23]. Ion velocities are determined by measuring the Doppler shift of the absorbing ions [24]. The $5d[4]_{7/2}$–$6p[3]_{5/2}$ transition has the added benefit of being easily accessible using a cw diode laser.

One drawback to this transition is that for the 19 isotopic and spin split components contributing to the hyperfine structure of the $5d[4]_{7/2}$–$6p[3]_{5/2}$ xenon ion transition, only the $6p[3]_{5/2}$ upper state has confirmed nuclear spin splitting constants [23, 25–27]. The hyperfine splitting constants characterize the small variations in state energies associated with the odd-numbered isotopes, which contribute to broadening in the measured spectral feature. This transition was first used by Manzella [28] to make velocity measurements in a Hall thruster plume. In that study, splitting constants for the similar $5d^4D_{7/2}$–$6p^4P_{5/2}$ transition at 605.1 nm were used in modeling the transition lineshape, and it was shown that Doppler broadening generally dominates the broadening

mechanisms in these types of plasmas. The $5d[4]_{7/2}$–$6p[3]_{5/2}$ has since been used throughout the electric propulsion community to characterize a variety of thrusters operating on xenon [14, 29, 30].

LIF measurements for this study were performed at the Air Force Research Laboratory (AFRL) Electric Propulsion Laboratory at Edwards AFB, CA. This experimental apparatus has been described extensively in previous work [29, 31]. Figure 3 shows a top view of the experimental set-up, including the thruster, one branch of the probe optics and the collection optics. The thruster is mounted on a system of orthogonal translation stages that allows for three axes of motion. The anode and cathode potentials are floating with respect to ground. The cathode is located to the side of the thruster opposite to the collection optics with the tip at a radial distance of 73 mm from the centreline and axial distance of 28 mm from the exit plane with its axis oriented at an angle of 70° degrees with respect to the outward normal to the exit plane, as is consistent with previous studies [10, 20, 21].

The laser is a New Focus Vortex TLB-6017 tunable diode laser, capable of tuning approximately ±50 GHz about a centre wavelength of 834.72 nm. The 10 mW beam is passed through several beam pick-offs followed by a 50–50 cube beam splitter (BS) where it is split into two beams of equal power, approximately 5 mW each. The axial probe beam, shown in both figures 3 and 4, is focused by a lens and enters the vacuum chamber through a window. The radial beam, shown in figure 4 only, is periscoped from the optical bench to the top of the chamber such that it enters the chamber from above the thruster and probes the velocity perpendicular to the axial beam. Each probe beam is chopped at a unique frequency by choppers Ch2 (2 kHz) and Ch3 (2.8 kHz) for phase sensitive detection of the fluorescence signals.

The two wedge BSs shown in figure 3 provide portions of the beam for wavelength and velocity calibration. These include use of a commercial wavelength meter and a 300 MHz free spectral range Fabry–Perot etalon (F–P) to monitor wavelength during a laser scan, and a low pressure xenon hollow cathode discharge lamp to provide a stationary absorption reference for the determination of the unshifted spectral line position (zero velocity reference). The xenon lamp has no detectable population of the ionic xenon $5d[4]_{7/2}$ state, therefore the nearby (estimated to be 18 GHz distant) neutral xenon $6s'[1/2]_1$–$6p'[3/2]_2$ transition at 834.68 nm [32, 33] is used for the reference.

The fluorescence collection optics are also shown in figure 3. The fluorescence is collected by a 75 mm diameter, 300 mm focal length lens within the chamber and oriented 60° from the probe beam axis. The plume divergence half angle has previously been measured as 70° for 90% of the integrated beam current. However, the peak ion flux lies between 30° and 40° and drops off by more than 75% by the 70° point [21]. By placing the LIF collection optics at 60° off this axis [29], it is possible to interrogate points along the centreline up to 20 mm inside the thruster acceleration channel, while keeping the lenses and mirrors away from much of the plume ion flux. In this way, it is possible to probe internal ion acceleration of the DCFT with minimal intrusion into the plume and without destroying the collection optics through sputtering. The collimated fluorescence signal is directed through a window in the chamber side wall to a similar lens that focuses the collected fluorescence onto the entrance slit of the 125 mm focal length monochromator with a photomultiplier tube (PMT) at its exit. Due to the 1 : 1 magnification of the collection optics, the spatial resolution of the measurements is determined by the geometry of the entrance slit (0.7 mm width and 1.5 mm height) as well as the sub-mm diameter of the probe beam.

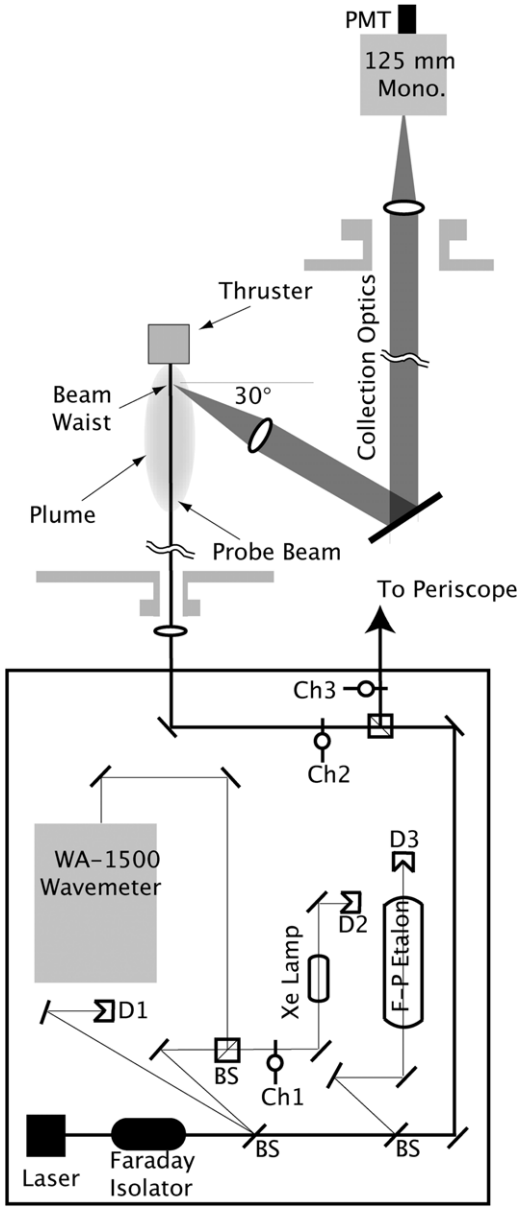

Figure 3. Top view diagram of the laser optical train and collection optics. Note that the radial probe beam periscope and focusing optics are not shown.

The combination of thruster geometry and collection optics allows for a large region of the DCFT channel and plume to be interrogated; however, lower S/N closer to the anode and along the centreline of the plume limit the measurements that are meaningful. The current density along the centreline of the thruster is far less than that seen in the jet between 30° and 40°.

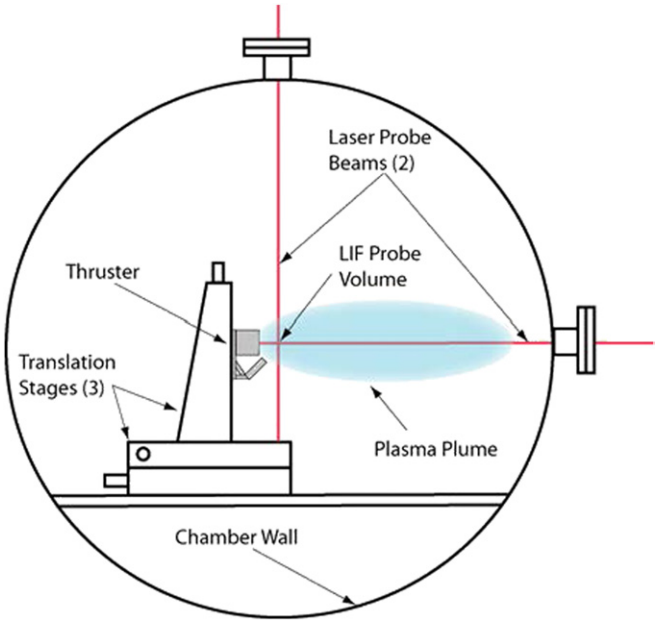

Figure 4. Side view diagram of thruster within AFRL chamber 6. Also shown are the translation stages and the laser probe beams. Note that the fluorescence collection and external optics are not shown.

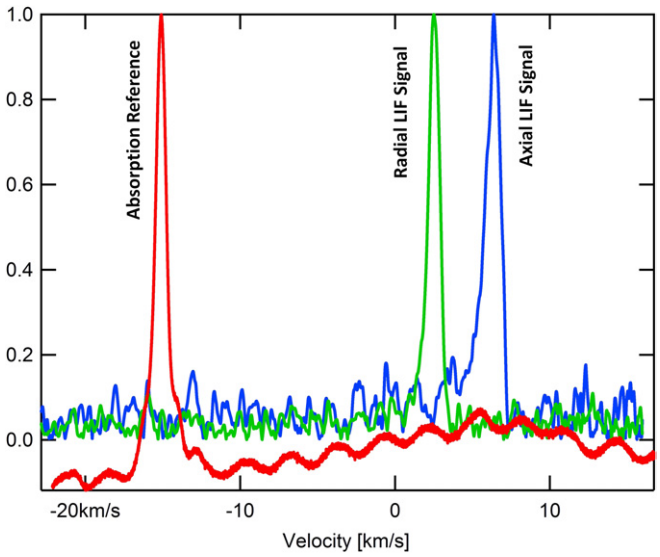

Figure 5. Example of LIF and absorption traces taken at $R = 4$ mm and $Z = 4$ mm, given for the low-current mode of operation. Note that 0 m s^{-1} is shown with respect to the 834.72 nm transition for a stationary ion.

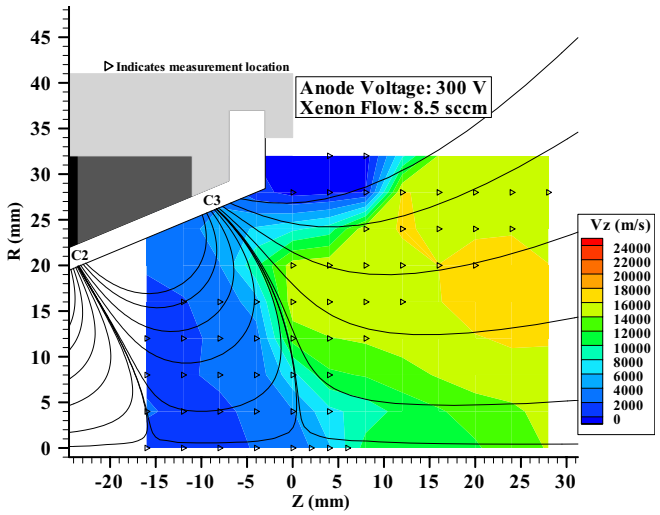

Figure 6. Contour plot of most probable axial ion velocities for the high-current operating condition, including magnetic field line overlay.

For the high-current mode, the centreline current density is a factor of two less than that in the jet, while for the low-current mode, it is a full order of magnitude less [21], creating a hollow plume. In this region, the S/N is much lower than in the jet, since the fluorescence signal strength is linearly dependent on the number density of excited ions [34].

The uncertainty of the velocity measurements is estimated to be ± 500 m s^{-1}. The fluorescence line shapes are often significantly broadened, presumably due to wide velocity distributions caused by plasma fluctuations. The quoted uncertainty should therefore be viewed as the repeatability in the determination of the peak of the fluorescence line shape. Measurements confirm that this combination of apparatus and laser power are well within the linear fluorescence regime.

3. Results and discussion

As described above, two operating conditions are presented in this study: a high-current mode, for which the anode discharge current is oscillatory; and a low-current mode for which the anode discharge is quiescent. The ion velocities presented in this study represent most probable (or peak) values calculated using the shift relative to the stationary reference in the LIF excitation profile, as shown in figure 5. At this point, VDFs are not extracted from the measured unsaturated lineshapes because we cannot say with certainty that the spectral lines are not significantly affected by Zeeman splitting. The most probable ion velocities are therefore used to show trends in the data, and in some cases to estimate the electric field from corresponding changes in kinetic energy.

The most probable ion velocities for both the high- and low-current conditions are presented as contour plots in figures 6 to 11. In each case, the magnetic field profile and location of the LIF measurements are overlaid. The magnetic field lines shown are for visualization of the field direction, and their spacing should not be taken as indicative of the varying magnetic field strengths. The contour plot was achieved by forming a rectangular grid with 4 mm spacing in the axial and radial directions, and using a weighted average dependent on the distance between points to interpolate the data. Therefore, the contours directly surrounding the data points can be considered to be most accurate, while those not surrounding data points (i.e. in the hollow centre of the plume) are meant only to continue the trends seen in the measurements.

3.1. High-current mode

Figures 6 to 8 show contour plots of the most probable xenon ion velocities measured for the high-current mode of operation.

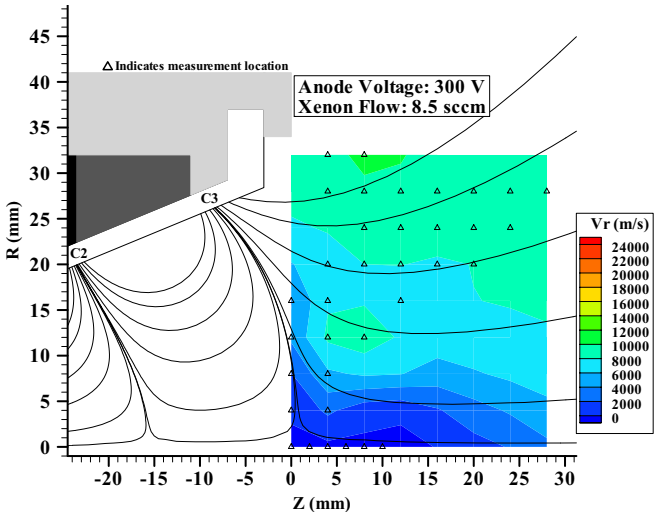

Figure 7. Contour plot of most probable radial ion velocities for the high-current operating condition, including magnetic field line overlay.

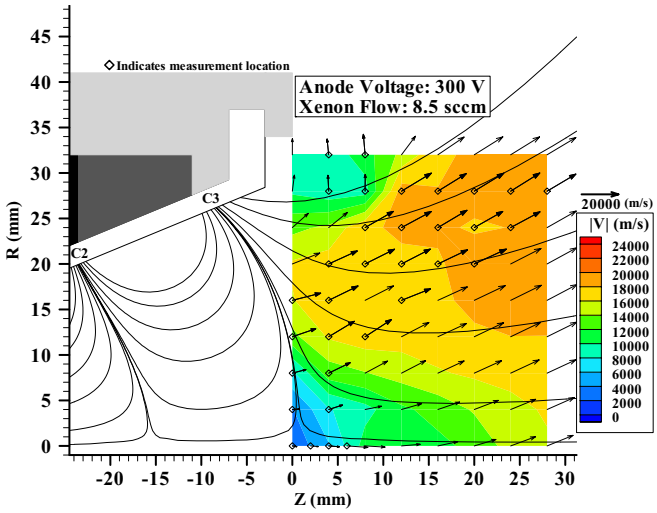

Figure 8. Contour plot of the magnitude of the total most probable ion velocities for the high-current operating condition, including magnetic field line overlay. Arrows indicate the direction of the velocities.

We see from figure 6 that the majority of the high-speed ions ($v > 15\,\mathrm{km\,s^{-1}}$) reside in the plume outside of the thruster, just beyond the third magnetic cusp. Rapid axial acceleration appears to occur perpendicular to the magnetic separatrix of this most downstream cusp. It is interesting to note that some acceleration occurs upstream of this point, most probably in the vicinity of the second cusp, although measurements were not able to be taken far enough upstream to resolve this region of the flow. It is also apparent that at any axial location, the ions are generally slowest near the centreline and faster at approximately 2/3 of the exit radius, with lines of constant velocity following along the separatrices of the last two cusps.

The contour plot of the radial velocities indicates that the highest radial velocities occur in the jet region of the plume at a radius of 25 mm or more off-axis. In this jet region, the radial velocities are of comparable magnitude to the axial velocities (e.g. around $16\,000\,\mathrm{m\,s^{-1}}$ axial, $10\,000\,\mathrm{m\,s^{-1}}$ radial), which is indicative of the highly divergent nature of cusped field thrusters. Along the centreline of the thruster, there is little to no radial velocity. This is in contrast to the CHT-30 thruster in which there appears to be a convergence of the velocity field towards the axis [7, 8, 14]. This also differs from the ion velocity fields seen in many traditional Hall thrusters [31] where there is a mixing region in front of the nosecone where ions from opposite sides of the annular thruster channel cross paths due to their inward-directed radial velocities originating along the channel centreline.

Figure 8 provides a contour plot of the overall magnitude of the ion velocity. Superimposed in this figure are vectors pointing along the local ion flow direction, the lengths of which are equal to the local ion speed. We see that close to the separatrix of the third cusp, the ion acceleration appears to be normal to the field line, suggesting that the field lines near the cusps represent lines of low parallel resistivity. This correlation between the direction of ion velocity and the direction normal to the field lines breaks down further downstream of the cusp, and by approximately 15 mm into the plume it appears that the ions begin to follow the divergent magnetic field. While it is tempting to believe that ions may be tied to the magnetic field by the nature of their trajectories, the relatively large ion Larmor radius (>0.1 m) in this region of the flow suggests that the ion trajectories are initially defined by the accelerations experienced further upstream, while still experiencing small corrections by the electrostatic influence of strongly magnetized electrons that are tied to the field lines further downstream of the cusps.

3.2. *Low-current mode*

The low-current mode of operation is achieved by lowering the anode flow rate as well as raising the applied anode potential. As mentioned above, the low-current mode operated without strong oscillations in the discharge current. The lower flow rate made the discharge visibly less bright than that of the high-current mode of operation, indicating that there are fewer xenon atoms occupying excited electronic states. This resulted in fewer positions from which data can be obtained with sufficiently high S/N to make meaningful measurements of velocity.

Figures 9 and 10 depict contour plots (with measurement locations and magnetic field lines superimposed) of the most probable axial and radial xenon ion velocities measured for the low-current mode of operation, respectively. Figure 11 gives the magnitude of the total ion velocity, with vectors indicating the direction of the flow. In general, the contour plots of the low-current mode of operation show some similar trends to those seen in the high-current mode. However, there are several ion velocity field characteristics that distinguish this low-current mode from its oscillatory, more diffuse counterpart. For example, an examination of figure 9 reveals that there is a more abrupt axial acceleration taking place along the separatrix of the third cusp. Upstream of this separatrix, the ion velocities seem to be very low, suggesting that in the low-current mode, less acceleration (if any) takes place near the second cusp.

An examination of figure 10 reveals that there are strong radial components to the ion velocity as close as 10 mm from

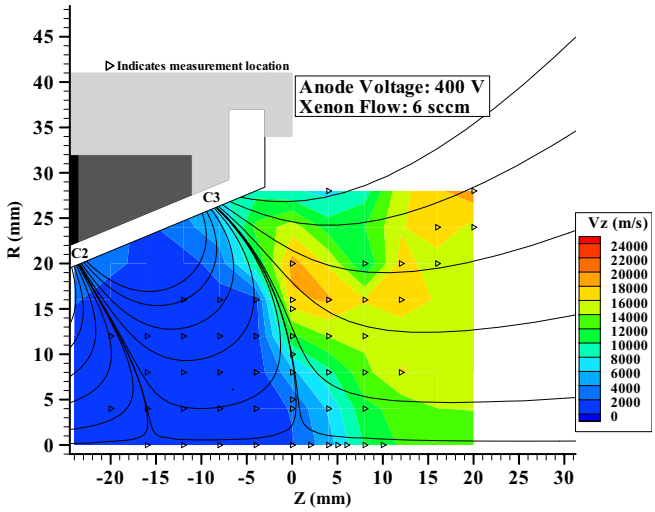

Figure 9. Contour plot of most probable axial ion velocities for the low-current operating condition, including magnetic field line overlay.

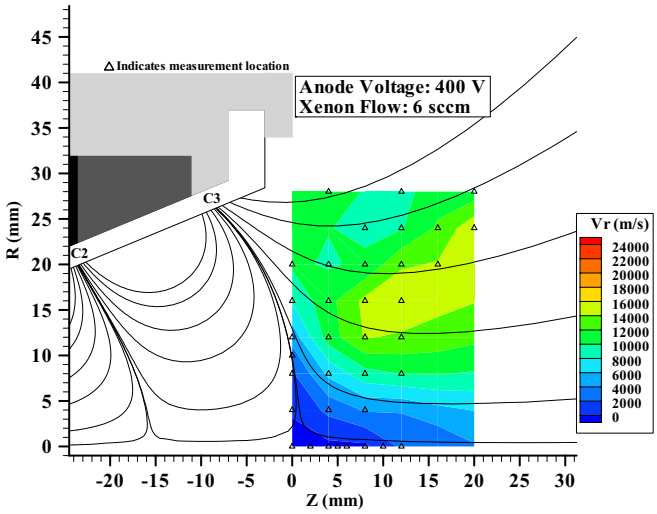

Figure 10. Contour plot of most probable radial ion velocities for the low-current operating condition, including magnetic field line overlay.

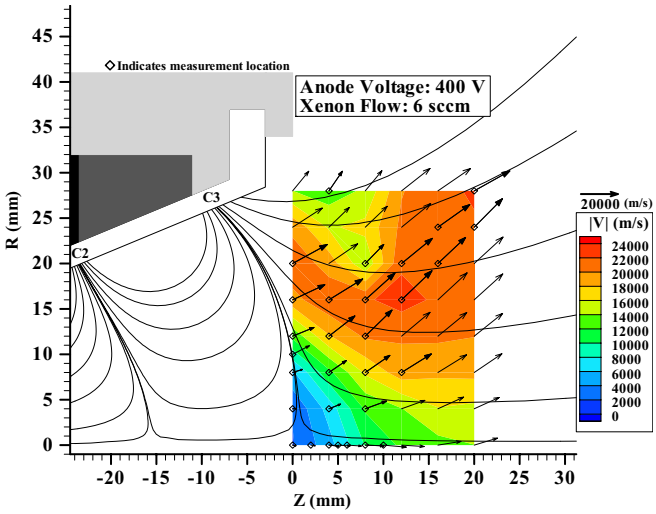

Figure 11. Contour plot of the magnitude of the total most probable ion velocities for the low-current operating condition, including magnetic field line overlay. Arrows indicate the direction of the velocities.

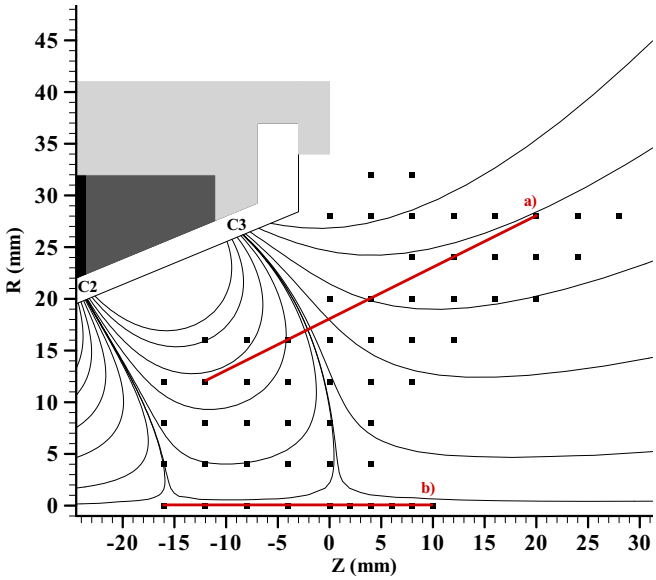

Figure 12. Locations of streamlines used to examine the axial kinetic energies and electric fields in the thruster plume.

the centreline. The development of a strong radial component so close to the axis results in a much stronger divergence of the ion beam (see figure 11), when compared with the flow field for the low-current mode depicted in figure 8. Visually comparing the thruster plumes, it appears that they have similar divergence half angles (between 30° and 40° [21]); however, the low-current mode shows a distinct, more luminous jet at this angle, whereas the high-current mode is luminous throughout the centre of the cone, not appearing as hollow.

The differences in velocity fields presented here must be interpreted with caution, as the LIF measurements are averaged over time. While the low-current mode has a quiescent discharge current, the high-current mode exhibits strong low frequency (≈3 kHz) [18] discharge current oscillations indicative perhaps of a fluctuation in the position of the ionization zone. Such a fluctuation can partially explain the deeper extension of the acceleration (closer to the second cusp) that is seen in this high-current mode, and the lower concentration of ion flux in the conical jet [21]. This behaviour would be best resolved with a time-dependent velocity diagnostic. Several studies have attempted such measurements by determining the time evolutions of ion velocity profiles after short interruptions to the thruster discharge power [35, 36]. For highly oscillatory discharges such as seen in the high-current mode of the DCFT, however, we propose that the time-dependent velocity diagnostic be directly synchronized to the discharge current oscillations and that the thruster be operated continuously.

3.3. Kinetic energy and electric fields

Two regions are examined in this study to determine the most probable axial ion kinetic energies and subsequently derived axial electric field. The first region, marked as (a) in figure 12, follows an approximate streamline in the jet

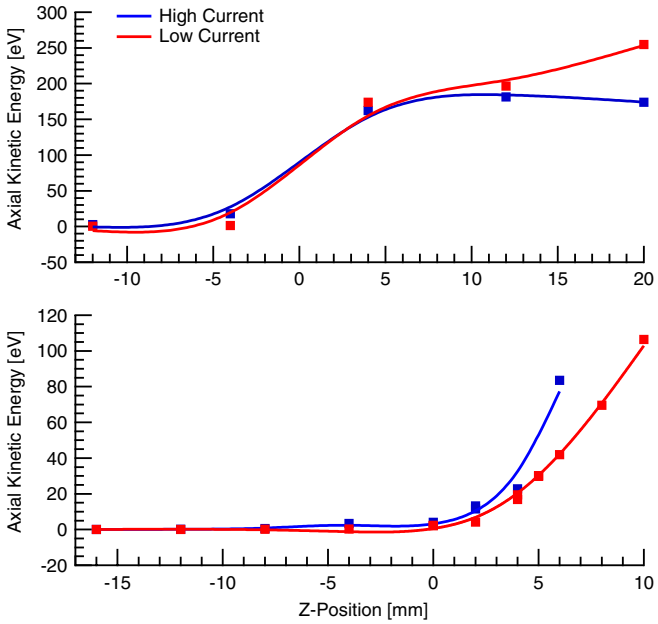

Figure 13. Axial kinetic energies derived from the most probable axial ion velocities along the jet region (top) and centreline (bottom) of thruster plume.

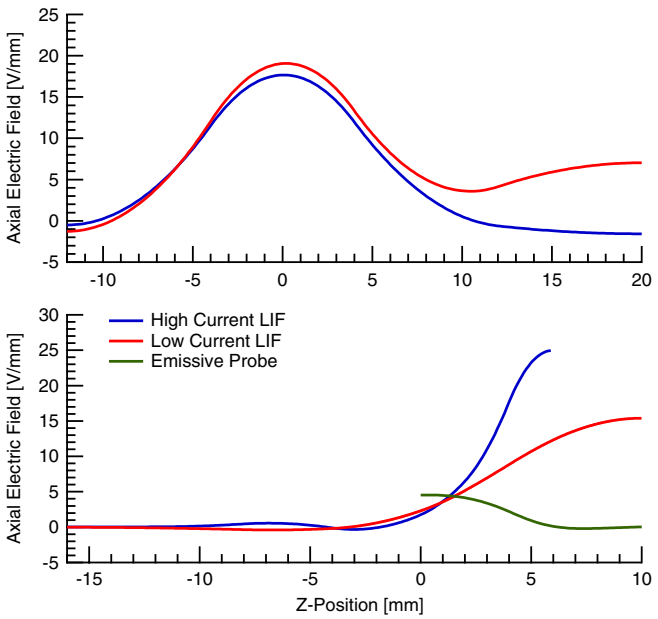

Figure 14. Axial electric fields derived from most probable kinetic energies along the jet region (top) and centreline (bottom) of the plume. The LIF derived electric fields are compared with the axial electric field derived from emissive probe plasma potential data.

region of the plume, determined by the arrows representing the flow directions in figures 8 and 11. Results along this streamline must be interpreted with caution, as the origins of ions along this path are not precisely known and may be distributed throughout the thruster channel. The second region, marked (b), is along the centreline of the thruster. It is more likely that ions born along the centreline continue along this path, as the radial velocities along the centreline are minimal.

Figure 13 depicts the variation in the most probable axial ion kinetic energy along the jet streamline and centreline of the thruster. Along the jet streamline, both high- and low-current modes appear to experience their largest axial accelerations starting inside the thruster channel at an axial position of approximately -4 mm. After +10 mm into the plume, the axial kinetic energies continue to increase for the low-current mode, while the high-current mode levels off. Along the centreline, the axial kinetic energies begin to increase rapidly at +2 mm into the plume for both operating conditions. For the high-current mode, however, the acceleration occurs more rapidly starting at approximately +4 mm. The tendency of the high-current mode having higher axial kinetic energy along the centreline of the plume, while the low current has higher values along the jet streamline, may be indicative of the differing plume structures for each mode (i.e. the high-current mode having high energy ions distributed more throughout the plume, while similar ions in the low-current mode are more restricted to the high-speed jet region).

Assuming that the ionization takes place upstream of the axial location where the acceleration is seen, the axial ion kinetic energies shown in figure 13 can be used to estimate the electric field. Figure 14 shows the implied axial electric fields corresponding to the paths along the jet and centreline streamlines. These data suggest that the vast majority of the potential drop occurs at the exit plane in the jet region, but potentially well beyond the exit plane (>+5 mm) along the centreline. It is noteworthy that preliminary emissive probe data taken along the centreline indicate that the region of strong electric field peaks very near the exit plane [19]. While probe measurements must be interpreted with caution as they are inherently intrusive, the discrepancy can also be attributed, at least partially, to the possibility that ionization is more distributed along the axis than what is assumed in generating the data in figure 14. However, the sudden acceleration that is defined by the increase in ion velocity at a location of approximately $Z = 0$ mm (exit plane), as depicted by figures 6, 9 and 13, is consistent with the location of where the separatrix from the third cusp intersects the thruster centreline, suggesting perhaps that this strong magnetic flux surface forms a barrier to electron transport, defining a resistance to electron flow and a potential barrier for ion acceleration. This is also true for where the separatrix crosses the path of the jet streamline.

4. Conclusions

Laser induced fluorescence was used to map the most probable ion velocities both inside the thruster channel and in the plume of the MIT developed DCFT. Two operating conditions were examined, including a high-current, oscillatory mode, and a low-current, quiescent mode. Contour plots of the most probable axial and radial ion velocities revealed several trends, including slower ions appearing inside the thruster channel near the centreline, with the fastest ions appearing after the separatrix formed at the third magnetic cusp. The magnetic field lines of this outermost separatrix appear to form lines of equal potential, with the majority of ion acceleration occurring near the exit plane in the plume of the thruster. Along the centreline of the thruster, the peak acceleration near the exit

plane is confirmed by the estimated electric field which showed that the peak potential drop occurs between 5 and 10 mm into the plume. Farther from the exit plane, the ion motion is indicative of ballistic trajectories that are no longer tied to the magnetic field lines.

The low-current mode showed a more abrupt axial acceleration at the third cusp separatrix than the high-current mode, and had stronger radial components of ion velocity closer to the centreline. These features caused the low-current mode of operation to have a more hollow, cone-shaped plume with a well contained jet at an angle between 30° and 40°, while the plume of the high-current mode was more diffuse. The diffuse plume appears to be related to the oscillatory nature of the high-current mode, in that the regions of ionization and acceleration may oscillate between the second and third cusps. To gain a better understanding of the differences between the high- and low-current modes, development of a laser-induced fluorescence measurement that is synchronized to the discharge current would be necessary to capture the dynamics of the thruster operation.

Acknowledgments

The authors would like to thank T Matlock, B Gregory, Lt A Campos and G Arzonia for their technical support. N MacDonald and S Gildea thank the Science Mathematics And Research for Transformation (SMART) scholarship programme for support of their research. Research at MIT and Stanford is funded through the Air Force Office of Scientific Research with Dr M Birkan as grant monitor.

References

[1] Goebel Dan M and Ira K 2008 *Fundamentals of Electric Propulsion: Ion and Hall Thrusters* (*JPL Space and Technology Series*) (New York: Wiley)

[2] Cappelli Mark A 2009 The Hall effect and rocket flight *Physics Today* (April) pp 76–7

[3] Kim V 1998 Main physical features and processes determining the performance of stationary plasma thrusters *J. Propul. Power* **14** 736–43

[4] Koch N, Harmann H P and Kornfeld G 2005 Development and test status of the thales high efficiency multistage plasma (HEMP) thruster family *Proc. 29th Int. Electric Propulsion Conf. (Princeton, NJ)* IEPC-2005-297

[5] Koch N, Harmann H P and Kornfeld G 2007 Status of the thales high efficiency multi stage plasma thruster development for HEMP-t 3050 and HEMP-t 30250 *Proc. 30th Int. Electric Propulsion Conf. (Florence, Italy)* IEPC-2007-110

[6] Raitses Y and Fisch N J 2001 Parametric investigations of a nonconventional Hall thruster *Phys. Plasmas* **8** 2579–86

[7] Raitses Y, Smirnov A and Fisch N J 2006 Cylindrical Hall thrusters *Proc. 37th AIAA Plasmadynamics and Lasers Conf. (San Francisco, CA)* AIAA 2006-3245

[8] Smirnov A, Raitses Y and Fisch N J 2007 Experimental and theoretical studies of cylindrical Hall thrusters *Phys. Plasmas* **14** 057106

[9] Raitses Y, Smirnov A and Fisch N J 2009 Effects of enhanced cathode electron emission on Hall thruster operation *Phys. Plasmas* **16** 057106

[10] Courtney D G and Martinez-Sanchez M 2007 Diverging cusped-field Hall thruster (DCHT) *Proc. 30th Int. Electric Propulsion Conf. (Florence, Italy)* IEPC-2007-39

[11] Young Christopher V, Smith Andrew W and Cappelli Mark A 2009 Preliminary characterization of a diverging cusped field (DCF) thruster *Proc. 31st Int. Electric Propulsion Conf. (Ann Arbor, MI)* IEPC-2009-166

[12] Bosch E and Flewry G 2004 Space twts today and their importance in the future *Proc. 22nd AIAA Int. Communications Satellite Systems Conf. and Exhibit 2004 (Monterey, CA)* AIAA 2004-3259

[13] Smirnov A, Raitses Y and Fisch N J 2005 The effect of magnetic field on the performance of low-power cylindrical Hall thrusters *Proc. 29th Int. Electric Propulsion Conf. (Princeton, NJ)* IEPC-2005-099

[14] MacDonald N A, Cappelli M A and Hargus W A Jr 2009 Laser-induced fluorescence velocity measurements of a low power cylindrical Hall thruster *Proc. 31st Int. Electric Propulsion Conf. (Ann Arbor, MI)* IEPC-2009-34

[15] MacDonald N A, Cappelli M A and Hargus W A Jr 2010 Ion velocity distribution in a low-power cylindrical Hall thruster *Proc. 46th AIAA/ASME/SAE/ASEE Joint Propulsion Conf. and Exhibit (Nashville, TN)* AIAA 2010-7103

[16] Courtney D G, Lozanoy P and Martinez-Sanchez M 2008 Continued investigation of diverging cusped field thruster *Proc. 44th AIAA/ASME/SAE/ASEE Joint Propulsion Conf. and Exhibit (Hartford, CT)* AIAA 2008-4631

[17] Matlock T, Daspit R, Batishchev O, Lozano P and Martinez-Sanchez M 2009 Spectroscopic and electrostatic investigation of the diverging cusped-field thruster *Proc. 45th AIAA/ASME/SAE/ASEE Joint Propulsion Conf. and Exhibit (Denver, CO)* AIAA 2009-4813

[18] Gildea S R, Matlock T S, Lozano P and Martinez-Sanchez M 2010 Low frequency oscillations in the diverging cusped-field thruster *Proc. 46th AIAA/ASME/SAE/ASEE Joint Propulsion Conf. and Exhibit (Nashville, TN)* AIAA 2010-7014

[19] Matlock T, Gildea S, Hu F, Becker N, Lozano P and Martinez-Sanchez M 2010 Magnetic field effects on the plume of a diverging cusped-field thruster *Proc. 46th AIAA/ASME/SAE/ASEE Joint Propulsion Conf. and Exhibit (Nashville, TN)* AIAA 2010-7104

[20] Courtney D G 2008 Development and characterization of a diverging cusped field thruster and a lanthanum hexaboride hollow cathode *Master's Thesis* Massachusettes Institute of Technology

[21] Gildea S R, Martinez-Sanchez M, Nakles M R, Hargus W A Jr 2009 Experimentally characterizing the plume of a divergent cusped-field thruster *Proc. 31th Int. Electric Propulsion Conf. (Ann Arbor, MI)* IEPC-2009-259

[22] Hansen J E and Persson W 1987 Revised analysis of singly ionized xenon, Xe II *Phys. Scr.* **36** 602–43

[23] Brostrom L, Kastberg A, Lidberg J and Mannervik S 1996 Hyperfine-structure measurements in Xe II *Phys. Rev.* A **53** 109–12

[24] Demtroeder W 1996 *Laser Spectroscopy: Basic Concepts and Instrumentation* (Berlin: Springer)

[25] Hargus W A Jr and Cappelli M A 2001 Laser-induced fluorescence measurements of velocity within a Hall discharge *Appl. Phys.* B **72** 961–9

[26] Geisen H, Krumpelmann T, Neuschafer D and Ottinger C 1988 Hyperfine splitting measurements on the 6265 Å and 6507 Å lines of seven Xe isotopes by LIF on a beam of metastable Xe($^3P_{0,3}$) atoms *Phys. Lett.* A **130** 299–309

[27] Fischer W, Huhnermann H, Kromer G and Schafer H J 1974 Isotope shifts in the atomic spectrum of xenon and nuclear deformation effects *Z. Phys.* **270** 113–20

[28] Manzella D H 1994 Stationary plasma thruster ion velocity distribution *Proc. 30th Joint Propulsion Conf. and Exhibit (Indianapolis, IN)* AIAA 1994-3141

[29] Hargus W A Jr and Nakles M R 2008 Ion velocity measurements within the acceleration channel of

low-power hall thruster *IEEE Trans. Plasma Sci.* **36** 1989–97

[30] Mazouffre S, Gawron D, Kulaev V and Sadehgi N 2008 Xe^+ ion transport in the crossed-field discharge of a 5-kW-class Hall effect thruster IEEE *Trans. Plasma Sci.* **36** 1967–76

[31] Hargus W A Jr and Charles C S 2008 Near exit plane velocity field of a 200-Watt Hall thruster *J. Propul. Power* **24** 127–33

[32] Miller M H and Roig R A 1973 Transition probabilities of Xe I and Xe II *Phys. Rev.* A **8** 480–6

[33] Moore C E 1952 *Atomic Energy Levels* vol II (Chromium through Niobium), Circular of the National Bureau of Standards 467 (Washington, DC: US Govt Printing Office)

[34] Eckbreth A C 1996 *Laser Diagnostics for Combustion Temperature and Species* 2nd edn (London: Gordon and Breach)

[35] Mazouffre S and Bourgeois G 2010 Spatio-temporal characteristics of ion velocity in a Hall thruster discharge *Plasma Sources Sci. Technol.* **19** 065018

[36] Pelissier B and Sadeghi N 1996 Time-resolved pulse-counting lock-in detection of laser induced fluorescence in the presence of a strong background emission *Rev. Sci. Instrum.* **67** 3405–10